Journal of Alloys and Compounds 509 (2011) 8944–8951

Contents lists available at ScienceDirect

Journal of Alloys and Compounds

journal homepage: www.elsevier.com/locate/jallcom

Influence of niobium doping on phase composition and defect-mediated photoluminescence properties of Eu^{3+}-doped TiO_2 nanopowders synthesized in Ar/O_2 thermal plasma

Chenning Zhang [a,b], Tetsuo Uchikoshi [a], Ji-Guang Li [a], Takayuki Watanabe [b], Takamasa Ishigaki [a,c,*]

[a] Materials Processing Unit, National Institute for Materials Science, Tsukuba, Ibaraki 305-0047, Japan
[b] Department of Environmental Chemistry and Engineering, Tokyo Institute of Technology, Yokohama, Kanagawa 226-8502, Japan
[c] Department of Chemical Science and Technology, Hosei University, Koganei, Tokyo 184-8584, Japan

ARTICLE INFO

Article history:
Received 26 February 2011
Received in revised form 20 June 2011
Accepted 21 June 2011
Available online 28 June 2011

Keywords:
Oxide materials
Gas–solid reactions
Rapid-solidification
Quenching
Phase transitions
Optical properties

ABSTRACT

Nb^{5+}:Eu^{3+}-codoped TiO_2 nanopowders for chemical composition adjustment have been synthesized via Ar/O_2 radio-frequency thermal plasma. X-ray diffraction (XRD) results reveal that all the resultant powders exhibited mixture polymorphs of anatase (mean size: ~45 nm) as the major phase and rutile (mean size: ~71 nm). Rutile formation was promoted by the Eu^{3+} doping but suppressed by the Nb^{5+} addition. Combined observation using FE-SEM and TEM indicates that all the plasma-synthesized powders had a majority of facet-shaped particles (several nanometers) and a small proportion of nearly spherical crystals (~150 nm). For the defect-mediated photoluminescence (PL) emission through the energy transfer from the TiO_2 host to the Eu^{3+} activator, the PL intensity originating from the $^5D_0 \rightarrow {}^7F_2$ electronic transition weakened but that from the $^5D_0 \rightarrow {}^7F_1$ electronic transition strengthened with increasing Nb^{5+} content. This may be a result of the decrease in the oxygen vacancy defects in the TiO_2 host lattice, as revealed by the joint means of UV–vis absorption spectra and excitation and emission spectra.

1. Introduction

Europium(III) is well known as an activator for bright red emission originating from its $^5D_0 \rightarrow {}^7F_2$ electronic transition, which has been widely used in some classical phosphors like Y_2O_3:Eu^{3+} [1–9] and Y_2O_2S:Eu^{3+} [10–13]. Titania (TiO_2) semiconductor exhibiting excellent thermal, chemical, and mechanical properties has been reported to be a promising candidate as a host material for the Eu^{3+} activator [14–20]. Since the direct excitation of the parity-forbidden intra-f-shell lanthanide ion crystal-field transitions is inefficient, most photoluminescence (PL) phosphors have primarily been targeted at the bright emission in the visible range under indirect excitation by ultraviolet (UV) light [21–27]. The PL emissions properties of Eu^{3+} ions arising from the energy transfer under UV light excitation in the TiO_2 host through a defect-mediated process have attracted increased attention in recent years. An important finding, by Frindell et al. [28], was that energy transfer could be achieved, enabling the observation of PL emission from the crystal field states to the Eu^{3+} ions, by exciting the TiO_2 host lattice within its band gap. In our previous work, Li et al. [29] utilized Ar/O_2 radio frequency (RF) thermal plasma to synthesize Eu^{3+}-doped TiO_2 luminescent nanocrystals. The synthesized powders had high crystallinity owing to the extremely high processing temperature (up to $\sim 1.5 \times 10^4$ K) [30], making it possible to significantly avoid the probability of hydroxyl formation, which generally occurs via the wet-chemical procedure and readily gives rise to nonradiative relaxations of rare-earth (RE) ions [31]. Therefore, the bright red emissions observed from the plasma-generated luminescent powders by indirectly exciting the TiO_2 host with the UV light were substantially confirmed to originate from efficient nonradiative energy transfer from the TiO_2 host to the Eu^{3+} activator through the defect-mediated process.

Much effort has been made to control the chemical composition in the synthesis of nanosized powders precisely and to functionalize them. We have already prepared functional nanosized TiO_2 powders doped with Fe^{3+} for photocatalysis [32], Fe^{3+} and Co^{2+} for magnetism [33,34], and Eu^{3+} and Er^{3+} for photoluminescence [29,35] via thermal plasma synthesis utilizing the pyrolysis of liquid precursors. The elemental compositions in these resultant powders have been proved to be almost equal to the prescribed amount in the precursor solutions. Recently, we have reported the synthesis of pure-phase nanocrystals in the full range of $BaTiO_3$–$SrTiO_3$ solid solution by thermal plasma upon adjusting the cation stoi-

* Corresponding author at: Department of Chemical Science and Technology, Hosei University, Koganei, Tokyo 184-8584, Japan. Tel.: +81 42 387 6134.
E-mail address: ishigaki@hosei.ac.jp (T. Ishigaki).

0925-8388/$ – see front matter © 2011 Elsevier B.V. All rights reserved.
doi:10.1016/j.jallcom.2011.06.089

chiometry in the liquid precursors and suppressing the formation of impurity phases [36].

As for the Eu^{3+}-doped TiO_2 luminescent powders, it is energy-mediating defects that are dominantly related to the oxygen defects generated in the TiO_2 host lattice [37]. In this respect, regulation of the oxygen defects caused by the Eu^{3+} doping by chemical composition adjustment in TiO_2 should affect the PL emission arising from the defect mediation.

In the present work, we used RF thermal plasma to synthesize Nb^{5+}:Eu^{3+}-codoped TiO_2 luminescent nanopowders with oxidizing mist precursor solution by using Nb^{5+} to regulate the oxygen vacancies in the TiO_2 host lattice arising from the Eu^{3+} doping. Highly precise control of the chemical composition was achieved in the synthesized oxide powder containing three metal elements (Nb, Eu, and Ti), even though the synthesis of materials composed of many elements is generally considered to be quite difficult in conventional methods, irrespective of phase: vapor or liquid. The Nb doping was found to influence the phase composition and the defect-mediated PL emission through energy transfer in the resultant powders. In the following sections, we report the synthesis process, phase composition, and PL properties.

2. Experimental

To prepare liquid precursors, a clear solution (A) was first obtained by adding 0.1 mol of titanium tetran-*n*-butoxide ($Ti(OC_4H_9)_4$, TTBO) (Wako Pure Chemical Industries Ltd., Tokyo, Japan) to 0.4 mol of diethanolamine ($HN(OC_2H_5)_2$, DEA) (Wako Pure Chemical Industries Ltd., Tokyo, Japan) under continuous magnetic stirring for 30 min. Here, DEA was used to prevent the hydrolysis of TTBO from intentionally added water or from exposure to moist air. Separately, niobium (V) ethoxide ($Nb(OC_2H_5)_5$) (Aldrich Ltd., Tokyo, Japan) (nominally, $Nb^{5+}/(Eu^{3+} + Nb^{5+} + Ti^{4+}) = 0$, 0.1, 0.2, 0.3, 0.5, 0.7, and 1.0 at.%) was injected into DEA in a prescribed amount (molar ratio of $Nb(OC_2H_5)_5$:DEA = 1:5), which also acted as a chelate for $Nb(OC_2H_5)_5$ against hydrolysis, to yield a solution (B). Europium(III) nitrate (Aldrich Ltd., Tokyo, Japan) (nominally, $Eu^{3+}/(Eu^{3+} + Nb^{5+} + Ti^{4+}) = 0$, 0.1, 0.2, 0.3, 0.5, 0.7, and 1.0 at.%) was dissolved in 20 ml of distilled water as a solution (C), with citric acid ($C_6H_8O_7$, CA, Eu^{3+}:CA = 1:1 in molar ratio) (Wako Pure Chemical Industries Ltd., Tokyo, Japan) as a chelate to make Eu^{3+} homogeneously disperse in water. Mixing solutions A, B, and C produced a stable clear solution as a liquid precursor.

For the synthesis of powders, synthesis processing via RF thermal plasma oxidization of the liquid precursor mists was conducted in an aerosol flow reactor. The plasma was generated in a water-cooled induction plasma torch (model PL-50, TEKNA Plasma System Inc., Sherbrooke, QC, Canada) using a 2 MHz RF power supply system (Nihon Koshuha Co. Ltd., Yokohama, Japan) operated at ~25 kW. The liquid precursor was delivered by a peristaltic pump to be injected axially into the plasma reactor as a mist through a water-cooled atomizer probe (model SA792-260-100, TEKNA Plasma System Inc., Sherbrooke, QC, Canada) at a feeding rate of 4.5 mL/min by 5 mL/min of argon carrier gas. Argon gas at 30 mL/min and a mixture gas of argon at 50 mL/min and oxygen at 40 mL/min were injected as central and sheath gases, respectively. Chamber pressure was controlled at ~500 Torr for 10 min, using an automatically adjustable vacuum pump system, to prevent the porous filter from being clogged by the plasma-generated powders during the reaction process. A detailed schematic of the experimental setup has been presented elsewhere [38].

Elemental concentrations of Eu^{3+} and Nb^{5+} in all the plasma-synthesized nanopowders were analyzed with an inductively coupled plasma optical emission spectrometer (ICP-OES: model SPS1700HVR, Seiko Instruments Inc., Chiba, Japan).

Phase identification was performed via X-ray diffraction (XRD) on a RINT 2200 X-ray diffractometer (Rigaku, Tokyo, Japan) using nickel-filtered Cu Kα radiation operating at 40 kV and 40 mA with a scanning speed of 0.5°/2θ per minute. All the XRD patterns were obtained through the operations of baseline subtraction, Lorentz polarization correction, and $K_{\alpha 2}$ stripping.

Average crystallite sizes (D) of rutile and anatase were estimated using the well-known Debye–Scherrer formula by analyzing the broadened rutile (1 1 0) and anatase (1 0 1) diffraction peaks, respectively [39].

The rutile weight fraction in the resultant powders was calculated from the integrated intensity of the diffraction peak in the XRD patterns, since the plasma-synthesized TiO_2 samples exclusively contained two phases of rutile and anatase, as proven in our previous work [33,40]. The equation for the rutile weight percentage calculation is [41]:

$$f_R = \frac{1}{1 + 0.79(I_A/I_R)} \quad (1)$$

where I_R and I_A are the integrated intensities of the rutile (1 1 0) and the anatase (1 0 1) peaks, respectively.

Particle morphology was observed using a field-emission scanning electron microscope (FE-SEM) (model S-5000, Hitachi, Tokyo, Japan) and a transmission electron microscope (TEM) with an acceleration voltage of 200 kV (JEM-2000 EX-II, Tokyo, Japan). The size distribution of the particles was then determined from the FE-SEM micrographs in image analyzer software, using the d_{50} value as the average particle size.

Absorption spectra were determined from ultraviolet–visible (UV–vis) spectra on a Jasco V-560 spectrophotometer (Jasco Co., Tokyo, Japan) with $BaSO_4$ used for baseline calibration. PL emission was produced via excitation using a Hitachi F-4500 fluorescence spectrophotometer (Hitachi, Tokyo, Japan) at room temperature with a 200 W Xe-lamp as an excitation source. The excitation spectra were corrected for the spectral distribution of the xenon lamp intensity by measuring Rhodamine-B as a reference, and the emission spectra were also corrected for the spectral response of a monochromator and Hamamatsu R928P photomultiplier tube by a light diffuser and a tungsten lamp (Noma, 10 V, 4 A). To accurately obtain the relative intensity of the PL emission through energy transfer, PL spectra were collected on a Renishaw spectrophotometer (Renishaw plc, Gloucestershire, UK) under 325 nm He–Cd laser excitation. Calibrations were made by subtracting the spectral responses of the PL equipment.

3. Results and discussion

It is confirmed in Table 1 that the nominal doping amounts of Eu^{3+} and Nb^{5+} in the precursor solutions were almost retained in the resultant powders. Hereafter, we use the nominal concentrations to indicate these plasma-synthesized powders. XRD patterns of some plasma-generated powders with typical addition contents are shown in Fig. 1. In all the cases, well-defined diffraction peaks indicate that the samples synthesized via RF thermal plasma had high crystallinity due to the extremely high synthesis temperature (~1.5×10^4 K) [30], indicating that there was little probability of the existence of hydroxyls affecting defect-mediated PL emission in this study. All the samples exhibited mixture polymorphs of anatase (JCPDS: No 84-1286) and rutile (JCPDS: No 78-2485). The appearance of metastable anatase as the major phase, even though the temperature in the plasma flame was as high as 1.5×10^4 K [30], is attributed to the fast quenching rate (~10^5–10^6 K/s) at the plasma tail as one of the promising characteristics in thermal plasma processing [30]. The metastable anatase as the major phase conformed well to the previous theoretical analysis through the critical free energy calculations for nucleation [42]. On the basis of the thermodynamic analysis in our previous work [42], in which we estimated the values of the interfacial energy between the condensed and liquid phase in pure TiO_2 system, it shows that the as-solidified phase

Table 1
Elemental concentrations of Eu^{3+} and Nb^{5+} in some randomly selected plasma-synthesized powders.

Nominal concentration in the precursor solutions		Measured concentration in the synthesized powders	
Eu/(Eu + Nb + Ti) (at.%)	Nb/(Eu + Nb + Ti) (at.%)	Eu/(Eu + Nb + Ti) (at.%)	Nb/(Eu + Nb + Ti) (at.%)
0.3	0.0	0.38	0.00
0.5	0.0	0.50	0.00
0.7	0.0	0.77	0.00
0.2	0.2	0.17	0.26
0.3	0.3	0.33	0.34
0.5	0.1	0.45	0.11
0.5	0.5	0.47	0.44
0.5	1.0	0.48	0.94

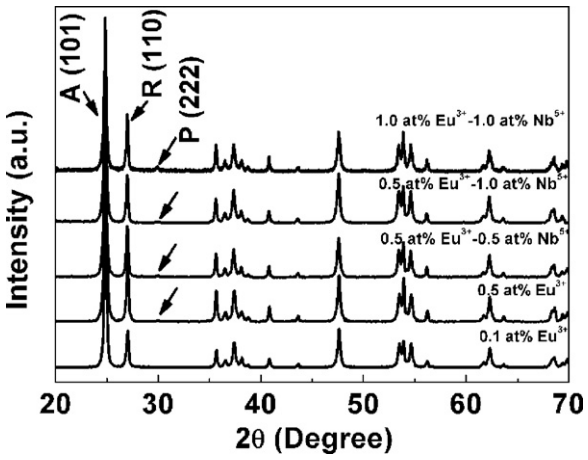

Fig. 1. XRD patterns of the plasma-synthesized powders with various addition contents of Eu^{3+} and Nb^{5+}. A, R, and P denote anatase, rutile, and $Eu_2Ti_2O_7$ pyrochlore, respectively.

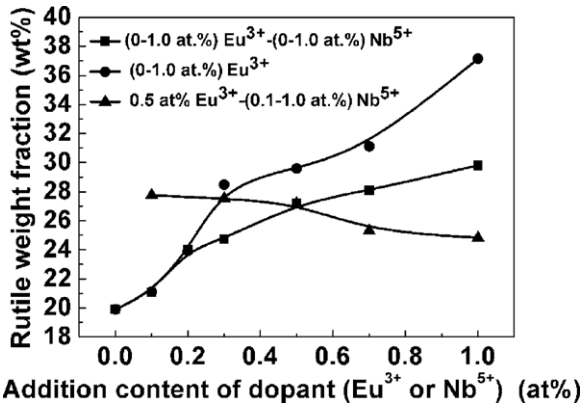

Fig. 2. Phase composition of the plasma-generated powders with varied dopant (Eu^{3+} or Nb^{5+}) contents (in the case of Eu^{3+}–Nb^{5+}, molar ratio of Nb^{5+}:Eu^{3+} = 1:1) as a function of dopant concentration.

depends on the solidification temperature or degree of supercooling of the TiO_2 melt. Through estimation, for a high cooling rate, we found that anatase nucleates directly from the melt below 2057 K, while rutile solidifies at a temperature close to the melting point, 2143 K, of TiO_2, indicating that the anatase is formed in a rapid cooling process and rutile is created under near-equilibrium solidification condition. According to classical homogeneous nucleation theory, the nucleation rate (I) in a supercooled melt is exponentially associated with the critical nucleation energy (ΔG^*) [43]:

$$I = A \exp\left(\frac{-\Delta G^*}{kT}\right) \quad (2)$$

where A is a pre-exponential factor related to the frequency of atom transport across the liquid–crystal interface, k is the Boltzmann constant, and T is the solidification temperature in Kelvin. According to this equation, the higher the critical nucleation energy, the slower the nucleation rate. Based on Skapski's theory of next-nearest neighbors [43], the maximum undercooling reaches $0.81T_m$, which indicates that homogenous nucleation can take place at temperatures ranging from $0.81T_m$ to the melting point T_m. By comparing the critical nucleation energies of anatase and rutile, we found that the value of $\Delta G^*_{rutile}/\Delta G^*_{anatase}$ is greater than 1 in the range of nucleation temperatures from $0.81T_m$ to T_m [44], indicating that the metastable anatase nucleates preferentially in that temperature range as the predominant phase in plasma-synthesized TiO_2.

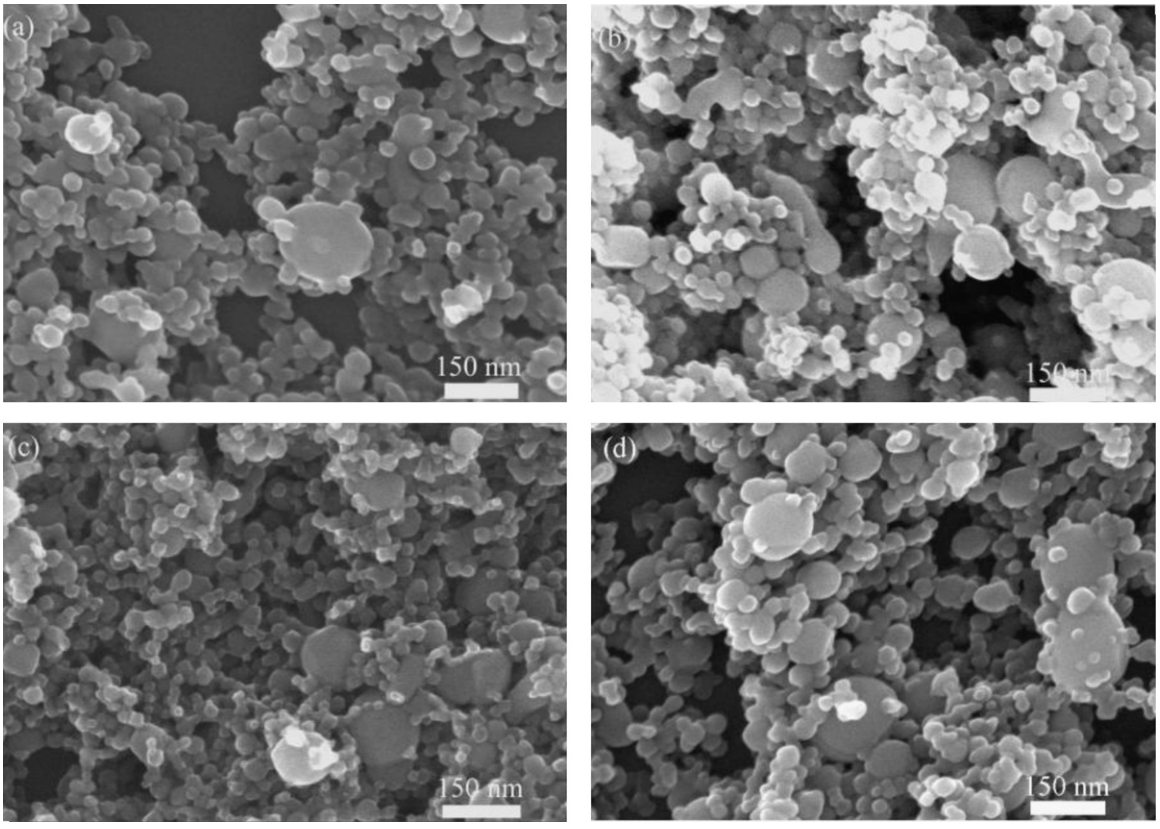

Fig. 3. Overall morphology of the plasma-synthesized powders: (a) undoped TiO_2, (b) (0.5 at.%) Eu^{3+}–TiO_2, (c) (0.5 at.%) Nb^{5+}–(0.5 at.%) Eu^{3+}–TiO_2, and (d) (1.0 at.%) Nb^{5+}–(0.5 at.%) Eu^{3+}–TiO_2.

Moreover, in our previous studies on TiO_2 synthesized by thermal plasma, we found similar experimental results for the phase composition in the resultant products, that is, mixture polymorphs of anatase as the main phase and rutile [29,33,35,38,45]. The average crystallite sizes of anatase and rutile in all the samples were estimated to be ~45 nm and ~71 nm, respectively. It was found that the mean particle size of rutile was generally larger than that of anatase, which can be explained from the thermodynamic analysis of the nucleation of anatase and rutile from TiO_2 melts [42]. Such a thermodynamic calculation showed that the nucleation of the anatase from the deeply undercooled TiO_2 occurred prior to that of the rutile from the less undercooled one, leading to larger rutile particles through more crystallite growth in the latter process. In the XRD patterns, the diffraction peak of $TiNb_2O_7$ phase (JCPDS: No 77-1374) in all the samples, which should obviously be located at $2\theta = 23.9^\circ$, could not be observed even up to 1.0 at.% of Nb^{5+}. This indicates the relatively high solubility for Nb^{5+} dissolving in the TiO_2 lattice [46] because of the effective ionic radius of Nb^{5+} (0.064 nm) being very close to that of Ti^{4+} (0.0605 nm) [47]. However, the slight stress in the TiO_2 host lattice was caused by the slightly bigger ionic radius of Nb^{5+} than that of Ti^{4+} [48]. In addition, no appreciable influence of the Nb^{5+} doping on improving the solubility of Eu^{3+} incorporated into the TiO_2 lattice could be found; that is, $Eu_2Ti_2O_7$ pyrochlore (JCPDS: No 23-1072) diffraction peak still appeared at 0.5 at.% of Eu^{3+}, like the case in the Eu^{3+}-singly doped powder, since excess Eu^{3+} was expelled during the superfast quenching at the plasma tail [29].

Fig. 2 shows rutile weight fractions in all the plasma-synthesized powders with various dopant concentrations; they were calculating according to Eq. (1). Comparing the samples of the Eu^{3+}-doped TiO_2 and Nb^{5+}:Eu^{3+}-codoped TiO_2 (molar ratio of Nb^{5+}:Eu^{3+} = 1:1), the rutile weight fraction in the latter sample was appreciably lower than that in the former at equal Eu^{3+} doping content, especially

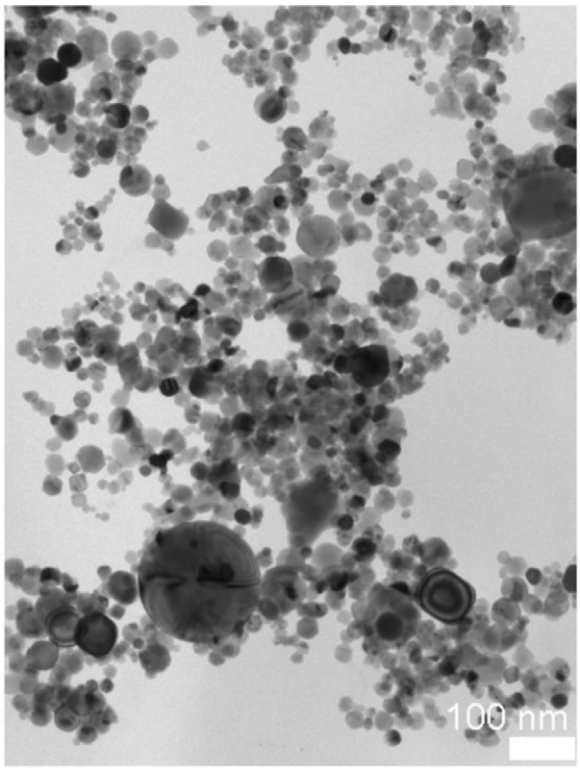

Fig. 4. TEM micrograph showing the morphology of the plasma-synthesized (0.1 at.%) Nb^{5+}:(0.5 at.%) Eu^{3+}-codoped TiO_2 powder.

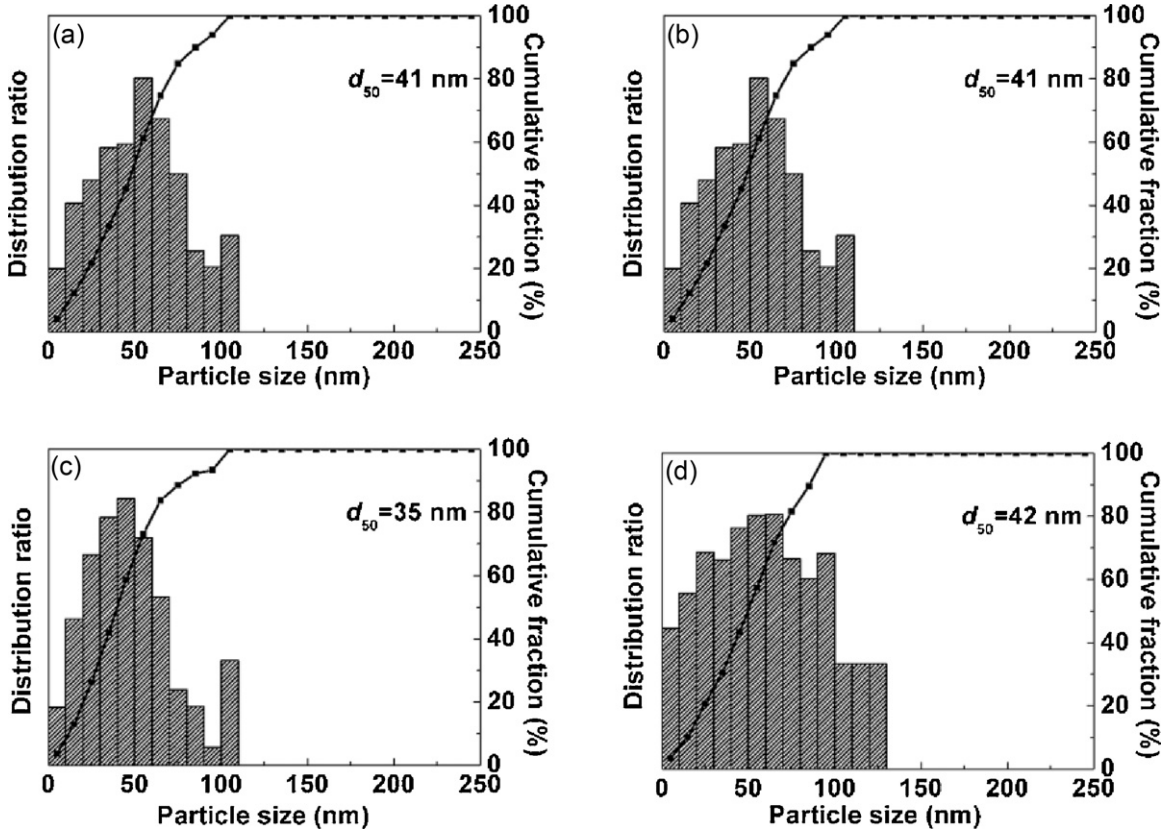

Fig. 5. Average crystallite size (d_{50}) and size distribution of the plasma-synthesized powders: (a) undoped TiO_2, (b) (0.5 at.%) Eu^{3+}–TiO_2, (c) (0.5 at.%) Nb^{5+}–(0.5 at.%) Eu^{3+}–TiO_2, and (d) (1.0 at.%) Nb^{5+}–(0.5 at.%) Eu^{3+}–TiO_2.

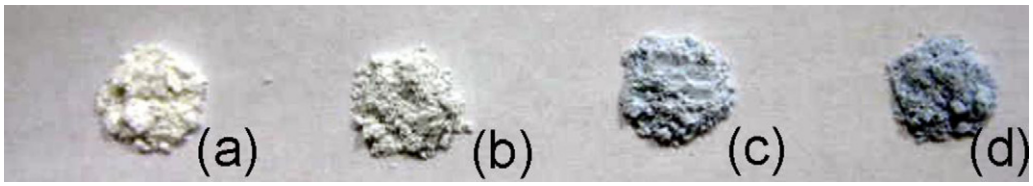

Fig. 6. Appearance of the plasma-synthesized powders with various dopant amounts: (a) undoped TiO_2, (b) (0.1 at.%) Nb^{5+}–(0.5 at.%) Eu^{3+}–TiO_2, (c) (0.5 at.%) Nb^{5+}–(0.5 at.%) Eu^{3+}–TiO_2, and (d) (1.0 at.%) Nb^{5+}–(0.5 at.%) Eu^{3+}–TiO_2.

at a relatively higher addition content of 1.0 at.% (37.1 wt.% in the former and 29.9 wt.% in the latter), indicating that the Nb^{5+} doping could effectively inhibit the formation of rutile. This phenomenon is attributed to the Nb^{5+} doping being able to contribute to the charge compensation for eliminating oxygen vacancies when subvalent Eu^{3+} was substituted into the TiO_2 host lattice. Oxygen vacancies have been known to favor rutile formation in TiO_2 gas clusters as a result of the chemical-valence discrepancy [49] between Eu^{3+} and Ti^{4+}. In the (0.1–1.0 at.%) Nb^{5+}:(0.5 at.%) Eu^{3+}-doped specimens, the rutile weight fractions steadily decreased with Nb^{5+} content from 27.8 wt.% at 0.1 at.% of Nb^{5+} content to 24.8 wt.% at 1.0 at.% of Nb^{5+} addition. Such a case further confirms that some oxygen vacancies could be successfully removed by offsetting the unbalanced charge between the Eu^{3+} and Ti^{4+} ions through the Nb^{5+} doping.

The morphology of the plasma-synthesized powders was revealed through extensive FE-SEM observation. Fig. 3 shows FE-SEM micrographs of some resultant samples with representative concentrations: (a) undoped TiO_2, (b) (0.5 at.%) Eu^{3+}–TiO_2, (c) (0.5 at.%) Nb^{5+}–(0.5 at.%) Eu^{3+}–TiO_2, and (d) (1.0 at.%) Nb^{5+}–(0.5 at.%) Eu^{3+}–TiO_2. They have similar morphologies, consisting of a majority of nanosized particles (several nanometers) assuming faceted shapes and a small proportion of submicrometer-sized crystals (~150 nm) appearing as nearly spheres. Such a morphology is displayed more clearly in a TEM micrograph of the (0.1 at.%) Nb^{5+}:(0.5 at.%) Eu^{3+}-codoped TiO_2 powder as a typical example (Fig. 4). This might be attributed with a high probability to distinctly different trajectories of the precursor mists in the thermal plasma synthesis process. Namely, fine particles were produced via the gas–solid route, while large ones were mainly formed via the gas–liquid–solid route.

In addition, the average particle sizes were estimated as d_{50} = 41, 38, 35, and 42 nm for samples (a)–(d), respectively, as demonstrated in Fig. 5. Such approximately close average particle sizes imply that the doping and/or codoping could not affect the resultant particle size appreciably in this work, suggesting that the size of synthesized powders should be principally governed by the parameter conditions during the thermal plasma synthesis, as they were fixed values in present study as already stated.

Fig. 6 illustrates color variation dependence of the Nb^{5+} doping concentration in the appearance of the undoped and (0.1, 0.5, and 1.0 at.%) Nb^{5+}:(0.5 at.%) Eu^{3+}-codoped TiO_2 powders. The deepening color associated with the rise in Nb^{5+} concentration indicates that Ti^{3+} ions were formed [50] owing to the introduction of Nb^{5+} into the TiO_2 host lattice, $(1/2)Nb_2O_5 + Ti_{Ti}^{\times} \rightarrow Nb_{Ti}^{\bullet} + Ti_{Ti}' + (5/4)O_2$, where Ti_{Ti} and Nb_{Ti} denote the titanium ions at titanium sites and niobium ions at titanium sites, respectively, and symbols $^{\bullet}$, $^{\times}$, and $'$ are the Kröger-Vink notation for net charge of +1, 0, and −1, respectively [51]. This reaction, however, was considered to occur in a reductive synthesis condition and high niobium concentration [52]. Thus, a reasonable explanation for the Ti^{3+} ions creation in the oxidative atmosphere in this work is that unlike the cases of TiN [53] and TiC [54] as starting materials in our previous work, the oxidation of the organic precursor generated various types of the gas species like CO (CO is more stable than CO_2 at the high

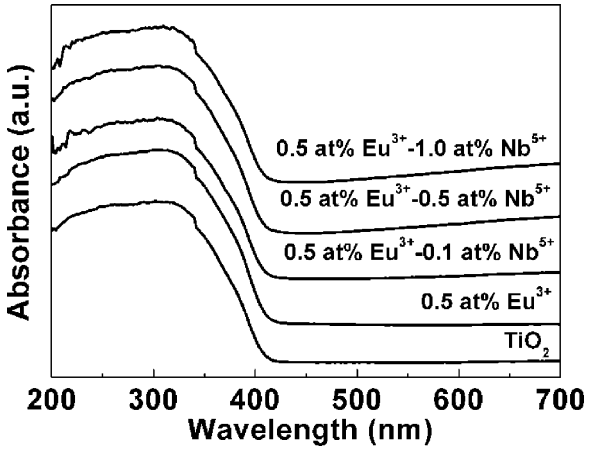

Fig. 7. UV–vis diffuse reflectance spectra of the plasma-synthesized powders with various adding concentrations of Eu^{3+} and Nb^{5+}.

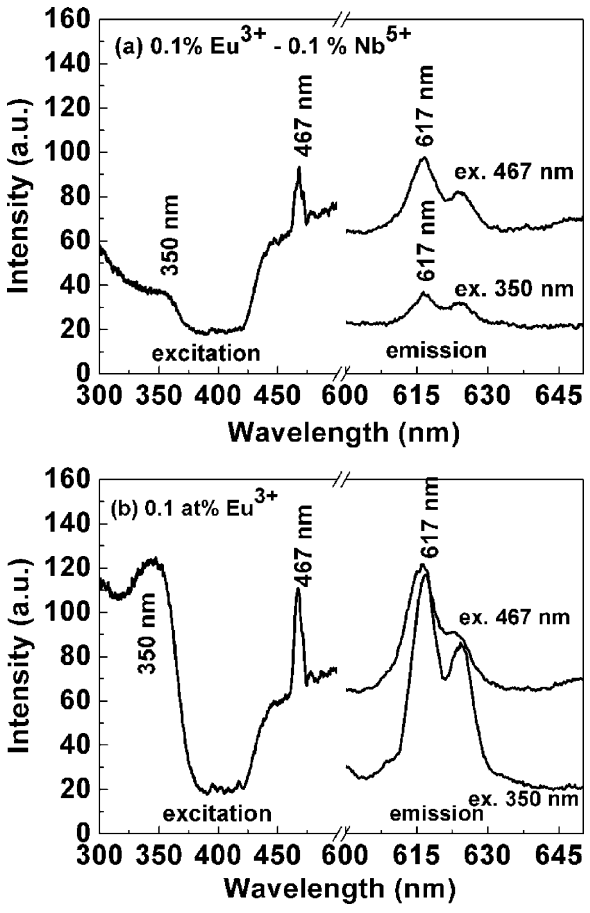

Fig. 8. Excitation (left side) and photoluminescence (PL) spectra (right side) of the plasma-synthesized powders: (a) (0.1 at.%) Nb^{5+}–(0.1 at.%) Eu^{3+}–TiO_2, (b) (0.1 at.%) Eu^{3+}–TiO_2. Peak wavelengths of the PL and the excitation (labeled ex.) are indicated, respectively.

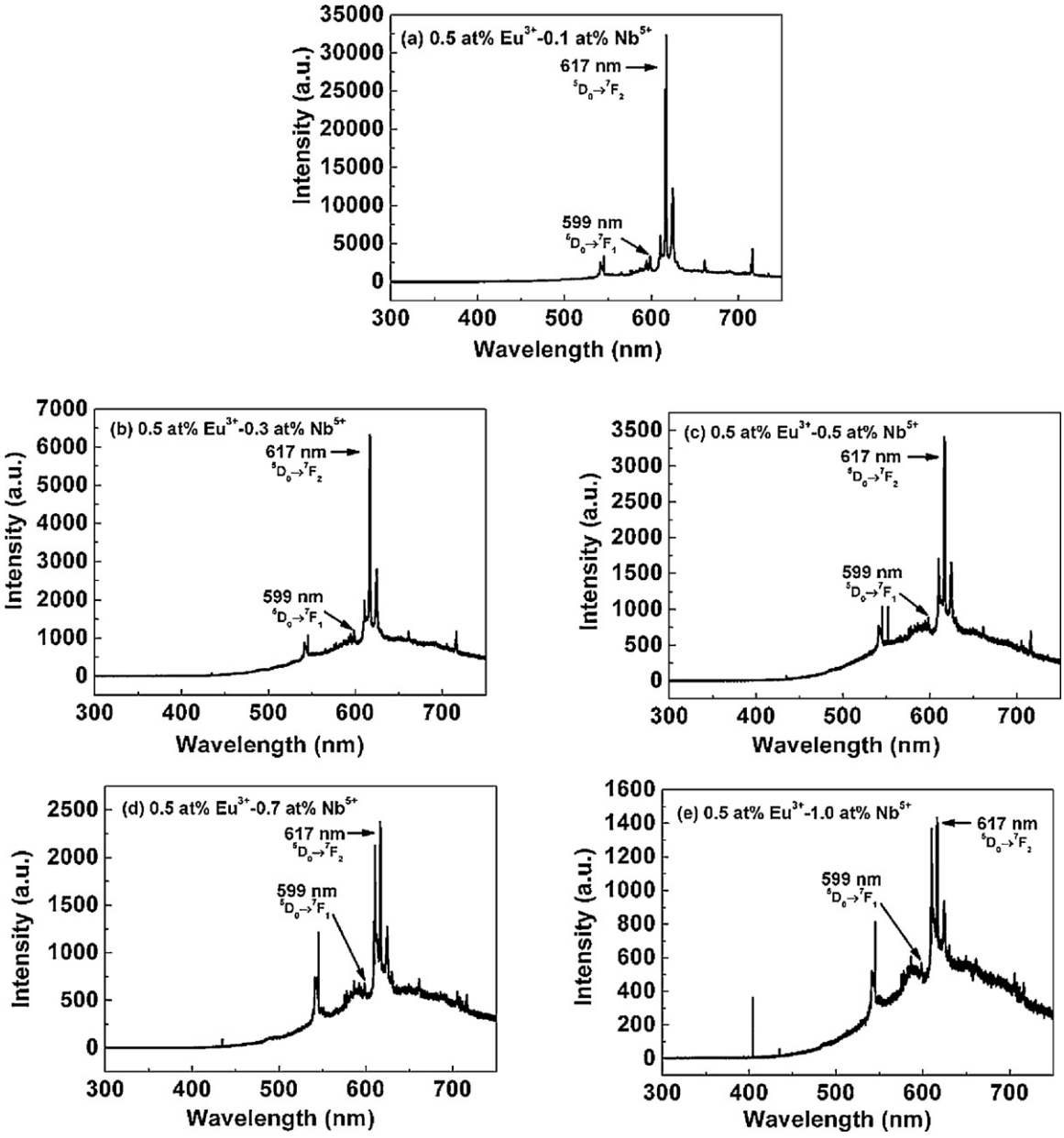

Fig. 9. Defect-mediated PL emission spectra of the (0.1–1.0 at.%) Nb^{5+}:(0.5 at.%) Eu^{3+}-codoped TiO_2 powders via thermal plasma synthesis. PL emission peaks are indicated.

temperature of thermal plasma), H_2O, and NO_x [45]; thus, a large amount of reducing CO gas provided a reductive atmosphere and the simultaneous release of huge amounts of the gases yielded a masking effect on O_2. This accounts for the presence of Ti^{3+} in the doped TiO_2 with Nb^{5+} even though the O_2 gas was input in the process of the thermal plasma. To reveal the presence evidence of Ti^{3+}, XPS spectra were determined for Degussa P25 commercial powder (Nippon Aerosil, Tokyo) and the plasma-synthesized samples of the undoped, 0.5 at.% Nb^{5+}:0.5 at.% Eu^{3+}-codoped, and 1.0 at.% Nb^{5+}:0.5 at.% Eu^{3+}-codoped TiO_2 powders. In the XPS profile of Ti 2p peak (not shown in the paper), compared with the cases of the P25 and undoped TiO_2, it is very difficult to distinguish the Ti^{3+} presence but quite weak Ti^{3+} traces in both the codoped powders because of the extremely small amount of Ti^{3+} arising from the low level of Nb^{5+} doping in this work.

UV–vis diffuse reflectance spectra of some plasma-synthesized powders are shown in Fig. 7. Note that data offsetting has been made here for overall clearness of the figure. Compared with the undoped and Eu^{3+}-doped TiO_2 powders, the introduction of Nb^{5+} could not significantly affect the absorption edge of the TiO_2 host in the codoped samples; that is, all the powders exhibited an onset of absorption at ~412 nm in the UV region. This is attributed to the relatively small amount of Nb^{5+} addition in this experiment, since the evident blue shift for the absorption edge of the TiO_2 host could be observed at a relatively large Nb^{5+} doping content as high as ~10 at.% [55] owing to the Burstein–Moss effect [56]. Additionally, the absorption peaks (beyond the TiO_2 absorption edge) of the Eu^{3+} activator, like 395, 416, 467, and 538 nm that are assignable to the intraconfigurational $4f \rightarrow 4f$ transitions of Eu^{3+} ions [57], were too weak to be detectable in this work, also owing to the relatively low Eu^{3+} addition content. Furthermore, the amount of Ti^{3+} formation arising from the Nb^{5+} addition was extremely low. As a result, the trivial number of Ti^{3+} ions residing at the surfaces of the resultant TiO_2 particles could not lead to higher absorption of visible light [38,58], namely, the redshift occurrence for the UV–vis absorption edge in Fig. 7.

Fig. 8 shows excitation and PL spectra of the plasma-synthesized powders: (a) (0.1 at.%) Nb^{5+}–(0.1 at.%) Eu^{3+}-codoped TiO_2 and (b)

(0.1 at.%) Eu^{3+}-doped TiO_2. For both the samples, the excitation spectra (left part in Fig. 8a and b) were determined to monitor the characteristic 617 nm red emission from the $^5D_0 \rightarrow {}^7F_2$ electronic transition of the Eu^{3+} ions. They presented a 350 nm broad peak corresponding to the absorption band of the TiO_2 host, as revealed by the UV–vis spectra in Fig. 7, and a 467 nm sharp peak assignable to $^7F_{0,1} \rightarrow {}^5D_2$ transition of Eu^{3+} activator [59]. These two excitation peaks indicate that the Eu^{3+} ions can be excited either indirectly through the TiO_2 host or directly through the Eu^{3+} ions themselves. However, it is notable that in Fig. 8a (right part), the PL (617 nm) intensity via the indirect excitation (350 nm) was considerably weaker than that via the direct excitation (467 nm) for the Nb^{5+}:Eu^{3+}-codoped TiO_2, which is unlike the case in which both the intensities are almost identical for (0.1 at.%) Eu^{3+}-doped TiO_2 in Fig. 8b (right part). Here, the photoluminescence emission produced by indirectly exciting the TiO_2 host lattice using 350 nm UV light originates from the energy transfer to sensitize the Eu^{3+} activator. The sensitization process was as follows: firstly, the energy of the UV light was absorbed by the TiO_2 band gap; then, the absorbed energy relaxed to the TiO_2 defect states; finally, the energy transferred to the crystal field states of the Eu^{3+} ions, exhibiting the photoluminescence emission. This energy transfer mechanism conforms to a model describing an energy level diagram in which UV light absorbed by the band gap of TiO_2 can be subsequently relaxed to the TiO_2 defect, followed by the energy transfer to the crystal field states of the RE ions, when the defect level is equal to or greater than the energy of the emitting state [28,60,61]. Moreover, it has been reported that the energy transfer process is successful only for some certain RE ions such as Sm^{3+}, Eu^{3+}, Yb^{3+}, Nd^{3+}, and Er^{3+} but not for the others like Tb^{3+} and Tm^{3+} [28].

Characteristic PL (617 nm) emission through energy transfer in the (0.1–1.0 at.%) Nb^{5+}:(0.5 at.%) Eu^{3+}-codoped TiO_2 powders via thermal plasma synthesis were thoroughly studied under 325 nm He–Cd laser excitation to highlight the influence of the Nb^{5+} doping on the defect-mediated PL properties of the luminescent powders, as shown in Fig. 9(a–e). In all the cases, a sharp PL peak at 617 nm definitely through the energy transfer from the TiO_2 host to the Eu^{3+} activator could be unambiguously observed via the 325 nm He–Cd laser beam irradiation. In the comparison of the PL emission peak under 325 nm laser excitation at 0.1–0.5 at.% of Eu^{3+} doping concentration in Fig. 9 with that of the $Eu_2Ti_2O_7$ reported in the literature [29], the major PL emission peak of the Eu^{3+} doped samples is relatively narrow and at a wavelength of approximately 617 nm, whereas that of the $Eu_2Ti_2O_7$ appears at around 610 nm with a relatively broad shape. Both cases imply that the Eu^{3+} activators existed

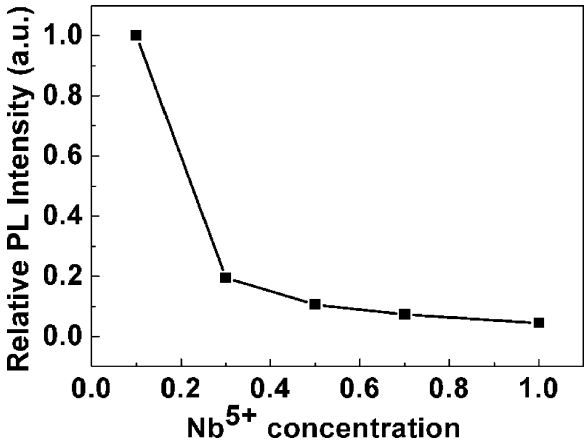

Fig. 10. Relative intensity of the defect-mediated PL emission as a function of varied Nb^{5+} concentration in the (0.1–1.0 at.%) Nb^{5+}:(0.5 at.%) Eu^{3+}-codoped TiO_2 powders (normalized).

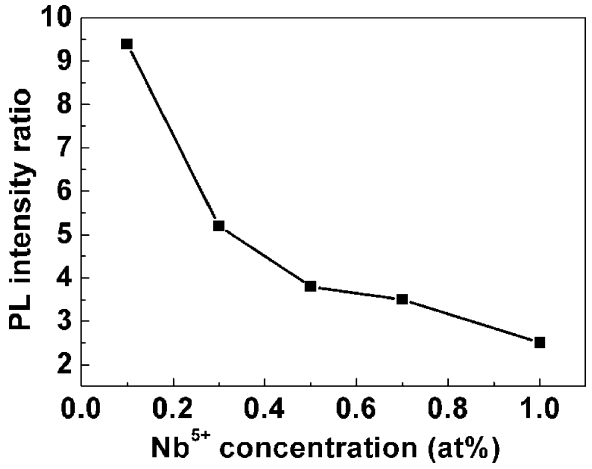

Fig. 11. Intensity ratio of the defect-mediated PL emissions of 617 nm ($^5D_0 \rightarrow {}^7F_2$) and 599 nm ($^5D_0 \rightarrow {}^7F_1$) as a function of varied Nb^{5+} concentration in the (0.1–1.0 at.%) Nb^{5+}:(0.5 at.%) Eu^{3+}-codoped TiO_2 powders.

in different host lattices; that is, in the former, the Eu^{3+} activator was located in the TiO_2 lattice as a result of the doping. It has been known that the $^5D_0 \rightarrow {}^7F_2$ line including Stark splits of the 617 nm emission originates from electric dipole transition. According to the Judd–Ofelt theory [62,63], the magnetic dipole transition is permitted while the electric dipole transition is forbidden. The electric dipole transition is allowed only on the condition that each Eu^{3+} ion occupies a site without an inversion center and is sensitive to local symmetry.

In this work, the electric dipole transition was much stronger than the magnetic dipole one, indicating that a Eu^{3+} ion occupied a low symmetry site without an inversion center in the TiO_2 host lattice. The substitution of Eu^{3+} for Ti^{4+} created oxygen vacancies and caused lattice distortion in the TiO_2 host, resulting in the site symmetry of Eu^{3+} deviating from the exact D_{2d} in anatase and D_{2h} in rutile [64]. As a result, the $^5D_0 \rightarrow {}^7F_2$ transition of Eu^{3+} dominated the emission spectra. However, relative PL intensity after normalization distinguishably reduced with the Nb^{5+} concentrations from 1.0 at 0.1 at.% of Nb^{5+} to 0.04 at 1.0 at.% of Nb^{5+} (Fig. 10), supporting the idea that the local symmetry of Eu^{3+} ions was improved by the Nb^{5+} doping, which was also evidenced from the decrease in the intensity ratio of the $^5D_0 \rightarrow {}^7F_2$ transition (monitored at 617 nm) to $^5D_0 \rightarrow {}^7F_1$ (monitored at 599 nm) in this study (Fig. 11), since the relative intensities of the $^5D_0 \rightarrow {}^7F_2$ and $^5D_0 \rightarrow {}^7F_1$ transitions are hypersensitive to the local symmetry of Eu^{3+} ions. This may be explained from the viewpoint that the number of oxygen vacancy defects resulting from the Eu^{3+} doping in the TiO_2 host lattice was decreased by the Nb^{5+} introduction, which has been proven by the inhibition of rutile crystallization as a contribution from the Nb^{5+} addition. In this case, the distortion of the TiO_2 lattice was alleviated, leading to the electric dipole transition becoming weak. On the other hand, the reduction in the number of defects gave rise to inefficient sensitization for the Eu^{3+} activator by exciton recombination in less defect mediation through the energy transfer from the TiO_2 host lattice under indirect excitation [37].

4. Conclusions

Nb^{5+}:Eu^{3+}-codoped TiO_2 nanopowders have been synthesized via RF thermal plasma. Precise adjustment of the codoping concentration in liquid precursors enables us to control the chemical composition of as-prepared nanosized powders. All the plasma-synthesized samples exhibited mixture polymorphs of anatase (major phase) and rutile. The average particle size of ~45 nm for the

anatase was generally smaller than that of ~71 nm for the rutile. The solubility limit (~0.5 at.%) of Eu^{3+} into TiO_2 was negligibly affected by the Nb^{5+} addition. Rutile formation was promoted by the Eu^{3+} doping but was suppressed by the Nb^{5+} addition. All the plasma-synthesized powders had a similar morphology with a majority of facet-shaped particles (several nanometers) and a small proportion of nearly spherical crystals (~150 nm). Defect-mediated PL intensity originating from the $^5D_0 \rightarrow {}^7F_2$ electronic transition weakened but that from $^5D_0 \rightarrow {}^7F_1$ electronic transition strengthened with increasing Nb^{5+} content.

Acknowledgments

We are grateful to Dr. Kenji Watanabe for characterization support for the Raman and PL measurement under laser excitation, to Dr. Rong-Jun Xie for the excitation and PL spectra, and to Satoshi Takenouchi and Takeshi Kobayashi for the chemical analysis. The support for the XPS measurement by Yoshiya Ueda of the Precision Analysis Laboratory of Hosei University is also acknowledged. This work was partially supported by Kakenhi, a Grant-in-Aid for Scientific Research (B 19360334) from the Japan Society for the Promotion of Science.

References

[1] V.B. Taxak, S.P. Khatkar, S.D. Han, R. Kumar, M. Kumar, J. Alloys Compd. 469 (2009) 224–228.
[2] Y.X. Fu, Y.H. Sun, J. Alloys Compd. 471 (2009) 190–196.
[3] C.N. Wang, W.P. Zhang, M. Yin, J. Alloys Compd. 474 (2009) 180–184.
[4] K.M. Nissamudeen, R.G.A. Kumar, V. Ganesan, K.G. Gopchandran, J. Alloys Compd. 484 (2009) 377–385.
[5] S.L. Zhong, J.J. Chen, S.P. Wang, Q.Y. Liu, Y.L. Wang, S.J. Wang, J. Alloys Compd. 493 (2010) 322–325.
[6] M.Z. Yang, Y. Sui, S.P. Wang, X.J. Wang, Y. Wang, S.C. Lu, T.Q. Lu, W.F. Liu, J. Alloys Compd. 509 (2011) 266–270.
[7] Y. Xiao, D.P. Wu, Y. Jiang, N. Liu, J.L. Liu, K. Jiang, J. Alloys Compd. 509 (2011) 5755–5760.
[8] X.C. Yan, R.B. Yu, D. Wang, J.X. Deng, J. Chen, X.R. Xing, Solid State Sci. 13 (2011) 1060–1064.
[9] X.S. Qu, B.A. Dong, G.H. Pan, X. Bai, Q.L. Dai, H. Zhang, R.F. Qin, H.W. Song, Chem. Phys. Lett. 509 (2011) 33–36.
[10] H.H. Zeng, X.M. Zhou, L. Zhang, X.P. Dong, J. Alloys Compd. 460 (2008) 704–707.
[11] W.Y. Li, Y.L. Liu, P.F. Ai, Mater. Chem. Phys. 119 (2011) 52–56.
[12] P.F. Ai, Y.L. Liu, W.Y. Li, L.Y. Xiao, Physica B 405 (2011) 3360–3364.
[13] P.F. Ai, Y.L. Liu, L.Y. Xiao, H.J. Wang, J.X. Meng, Sci. Technol. Adv. Mater. 11 (2010) 035002.
[14] Y.R. Wang, Y.J. Guo, G.J. Wang, F. Wang, J. Nanosci. Nanotechnol. 11 (2011) 3162–3170.
[15] H. Hafez, J.H. Wu, Z. Lan, Q.H. Li, G.X. Xie, J.M. Lin, M.L. Huang, Y.F. Huang, Nanotechnology 21 (2010) 415201.
[16] J.H. Huang, P.Y. Hung, S.F. Hu, R.S. Liu, J. Mater. Chem. 20 (2010) 6505–6511.
[17] J.J. Wu, X.J. Lu, L.L. Zhang, Y.J. Xia, F.Q. Huang, F.F. Xu, J. Alloys Compd. 496 (2010) 234–240.
[18] X.A. Feng, L. Yang, N.C. Zhang, Y.L. Liu, J. Alloys Compd. 506 (2010) 728–733.
[19] H.G. Zhao, C.W. Jia, H.G. Duan, Z.W. Sun, X.M. Wang, E.Q. Xie, J. Alloys Compd. 455 (2008) 497–500.
[20] R.S. Ningthoujam, V. Sudarsan, R.K. Vatsa, R.M. Kadam, Jagannath, A. Gupta, J. Alloys Compd. 486 (2009) 864–870.
[21] X. Zhang, Z. Zhang, H.J. Seo, J. Alloys Compd. 509 (2011) 4875–4877.
[22] C.F. Guo, Y. Xu, X. Ding, M. Li, J. Yu, Z.Y. Ren, J.T. Bai, J. Alloys Compd. 509 (2011) L338.
[23] N. Dhananjaya, H. Nagabhushana, B.M. Nagabhushana, B. Rudraswamy, C. Shivakumara, R.P.S. Chakradhar, J. Alloys Compd. 509 (2011) 2368–2374.
[24] Z.G. Cui, R.G. Ye, D.G. Deng, Y.J. Hua, S.L. Zhao, G.H. Jia, C.X. Li, S.Q. Xu, J. Alloys Compd. 509 (2011) 3553–3558.
[25] S.S. Yao, Y.Y. Li, L.H. Xue, Y.W. Yan, J. Alloys Compd. 491 (2010) 264–267.
[26] L.Y. Xiao, Q. Xiao, Y.L. Liu, P.F. Ai, Y.D. Li, H.J. Wang, J. Alloys Compd. 495 (2010) 72–75.
[27] W.T. Sun, Y.X. Gu, Q.H. Zhang, Y.G. Li, H.Z. Wang, J. Alloys Compd. 493 (2010) 561–564.
[28] K.L. Frindell, M.H. Bartl, M.R. Robinson, G.C. Bazan, A. Popitsch, G.D. Stucky, J. Solid State Chem. 172 (2003) 81–88.
[29] J.G. Li, X.H. Wang, K. Watanabe, T. Ishigaki, J. Phys. Chem. B 110 (2006) 1121–1127.
[30] T. Ishigaki, J.G. Li, Sci. Technol. Adv. Mater. 8 (2007) 617–623.
[31] A. Patra, C.S. Friend, R. Kapoor, P.N. Prasad, Chem. Mater. 15 (2003) 3650–3655.
[32] X.H. Wang, J.G. Li, H. Kamiyama, Y. Moriyoshi, T. Ishigaki, J. Phys. Chem. B 110 (2006) 6804–6809.
[33] X.H. Wang, J.G. Li, H. Kamiyama, M. Katada, N. Ohashi, Y. Moriyoshi, T. Ishigaki, J. Am. Chem. Soc. 127 (2005) 10982–10990.
[34] J.G. Li, R. Buechel, M. Isobe, T. Mori, T. Ishigaki, J. Phys. Chem. C 113 (2009) 8009–8015.
[35] J.G. Li, X.H. Wang, C.C. Tang, T. Ishigaki, S. Tanaka, J. Am. Ceram. Soc. 91 (2008) 2032–2035.
[36] N. Kobayashi, T. Ishigaki, T. Watanabe, J.G. Li, Int. J. Appl. Ceram. Technol., in press, doi:10.1111/j.1744-7402.2010.02546.x.
[37] T. Tachikawa, T. Ishigaki, J.G. Li, M. Fujitsuka, T. Majima, Angew. Chem. Int. Ed. 47 (2008) 5348–5352.
[38] J.G. Li, M. Ikeda, C.C. Tang, Y. Moriyoshi, H. Hamanaka, T. Ishigaki, J. Phys. Chem. B 111 (2007) 18018–18024.
[39] B. Cullity, S. Stock, Elements of X-Ray Diffraction, 3rd ed., Prentice-Hall Inc., New Jersey, 2001.
[40] J.G. Li, M. Ikeda, R. Ye, Y. Moriyoshi, T. Ishigaki, J. Phys. D: Appl. Phys. 40 (2007) 2348–2353.
[41] R.A. Spurr, H. Myers, Anal. Chem. 29 (1957) 760–762.
[42] Y.L. Li, T. Ishigaki, J. Cryst. Growth 242 (2002) 511–516.
[43] A.S. Skapski, Acta Metall. 4 (1956) 583–585.
[44] T. Ishigaki, J. Ceram. Soc. Jpn. 116 (2008) 462–470.
[45] J.G. Li, H. Kamiyama, X.H. Wang, Y. Moriyoshi, T. Ishigaki, J. Eur. Ceram. Soc. 26 (2006) 423–428.
[46] C. Zhang, M. Ikeda, T. Uchikoshi, J.G. Li, T. Watanabe, T. Ishigaki, J. Mater. Res. 26 (2011) 658–671.
[47] R.D. Shannon, Acta Crystallogr. A 32 (1976) 751–767.
[48] R.K. Sharma, M.C. Bhatnagar, Sens. Actuators B: Chem. 56 (1999) 215–219.
[49] R.D. Shannon, J.A. Pask, J. Am. Ceram. Soc. 48 (1965) 391–398.
[50] C. Di Valentin, G. Pacchioni, A. Selloni, J. Phys. Chem. C 113 (2009) 20543–20552.
[51] F.A. Kröger, H.J. Vink, Solid State Phys. 3 (1956) 307–435.
[52] A.M. Ruiz, G. Dezanneau, J. Arbiol, A. Cornet, J.R. Morante, Chem. Mater. 16 (2004) 862–871.
[53] S.M. Oh, J.G. Li, T. Ishigaki, J. Mater. Res. 20 (2005) 529–537.
[54] Y.L. Li, T. Ishigaki, J. Phys. Chem. B 108 (2004) 15536–15542.
[55] P.V. Kamat, N.M. Dimitrijevic, A.J. Nozik, J. Phys. Chem. 93 (1989) 2873–2875.
[56] A.V. Emeline, Y. Furubayashi, X. Zhang, M. Jin, T. Murakami, A. Fujishima, J. Phys. Chem. B 109 (2005) 24441–24444.
[57] H. Xin, R. Ma, L. Wang, Y. Ebina, K. Takada, T. Sasaki, Appl. Phys. Lett. 85 (2004) 4187–4189.
[58] C.D. Lokhande, E.H. Lee, K.D. Jung, O.S. Joo, J. Mater. Sci. 39 (2004) 2915–2918.
[59] K. Riwotzki, M. Haase, J. Phys. Chem. B 102 (1998) 10129–10135.
[60] G.A. Crosby, R.E. Whan, R.M. Alire, J. Chem. Phys. 34 (1961) 743–748.
[61] S. Sato, M. Wada, Bull. Chem. Soc. Jpn. 43 (1970) 1955–1962.
[62] B.R. Judd, Phys. Rev. 127 (1962) 750–761.
[63] G.S. Ofelt, J. Chem. Phys. 37 (1962) 511–520.
[64] R.A. Evarestov, V.P. Smirnov, Phys. Status Solidi B 215 (1999) 949–956.